Anisotropic impurity states, quasiparticle scattering and nematic transport in underdoped Ca(Fe$_{1-x}$Co$_x$)$_2$As$_2$

M. P. Allan[1,2,3], T-M. Chuang[2,3,4,5], F. Massee[2,3,6], Yang Xie[2], Ni Ni[7,8], S. L. Bud'ko[7,8], G. S. Boebinger[5], Q. Wang[9], D. S. Dessau[9], P. C. Canfield[7,8], M. S. Golden[6] and J. C. Davis[2,3,10,11]★

Iron-based high-temperature superconductivity develops when the 'parent' antiferromagnetic/orthorhombic phase is suppressed, typically by introduction of dopant atoms[1]. But their impact on atomic-scale electronic structure, although in theory rather complex[2-13], is unknown experimentally. What is known is that a strong transport anisotropy[14-25] with its resistivity maximum along the crystal b axis[14-25], develops with increasing concentration of dopant atoms[14,20-25]; this 'nematicity' vanishes when the parent phase disappears near the maximum superconducting T_c. The interplay between the electronic structure surrounding each dopant atom, quasiparticle scattering therefrom and the transport nematicity has therefore become a pivotal focus[7,8,12,22,23] of research into these materials. Here, by directly visualizing the atomic-scale electronic structure, we show that substituting Co for Fe atoms in underdoped Ca(Fe$_{1-x}$Co$_x$)$_2$As$_2$ generates a dense population of identical anisotropic impurity states. Each is ~8 Fe–Fe unit cells in length, and all are distributed randomly but aligned with the antiferromagnetic a axis. By imaging their surrounding interference patterns, we further demonstrate that these impurity states scatter quasiparticles in a highly anisotropic manner, with the maximum scattering rate concentrated along the b axis. These data provide direct support for the recent proposals[7,8,12,22,23] that it is primarily anisotropic scattering by dopant-induced impurity states that generates the transport nematicity; they also yield simple explanations for the enhancement of the nematicity proportional to the dopant density[14,20-25] and for the occurrence of the highest resistivity along the b axis[14-25].

Commensurate antiferromagnetism with orthorhombic crystal symmetry exists in the phase 'parent' to the superconductivity in most underdoped FeAs materials. The a axis unit cell is fractionally longer than that of the b axis, with the Fe spins aligning in an anti-parallel fashion along the a axis but parallel along the b axis. Doping is usually achieved by substitution of x transition-metal atoms per Fe. When $x \sim 4 \pm 1\%$, the superconductivity appears, reaching its maximum T_c usually near $x_c \sim 8 \pm 1\%$ (Fig. 1a), where the antiferromagnetic/orthorhombic phase disappears. A broken discrete rotational symmetry of both the crystal structure and the electronic characteristics precedes or coincides with the appearance of antiferromagnetism (Fig. 1a); this phenomenon is often referred to as a nematic phase or as electronic nematicity. And, indeed, a wide variety of techniques, including spectroscopic imaging scanning tunnelling microscopy[26-28] (SI-STM), d.c. electrical transport[14-16,19-22,24,25] (DCT), frequency-dependent electrical conductivity[17,18,23] (ACT), torque magnetometry[29] and angle-resolved photoemission[30,31] (ARPES) find intense, but unexplained, electronic nematicity in underdoped FeAs materials.

Before bulk detwinning of FeAs crystals was available, the only way to investigate electronic nematicity was by direct electronic structure imaging. This approach allowed discovery and atomic-scale visualization of electronic nematicity[26] in Ca(Fe$_{1-x}$Co$_x$)$_2$As$_2$ crystals[32-34]. The subsequent development of crystal detwinning revealed a spectacular, and strongly doping-dependent, transport anisotropy in the same part of the phase diagram[14,15]. To understand the relationship between the atomic-scale nematicity observed by direct visualization[26], and the transport anisotropy[14-25], has therefore become an urgent focus of research into the phase diagrams of iron-based superconductors.

We pursue these objectives by using spectroscopic imaging STM to study Ca(Fe$_{1-x}$Co$_x$)$_2$As$_2$ samples with $0 \leq x \sim 6\%$. These samples exhibit the expected suppression of antiferromagnetism and emergence of superconductivity. For Ca(Fe$_{1-x}$Co$_x$)$_2$As$_2$, the phase diagram actually depends on the annealing procedure[34]; samples that are annealed at high temperatures exhibit a collapsed tetragonal phase whereas samples annealed at low temperatures (or pristine samples as used here) show the typical phase diagram of 122 FeAs superconductors, albeit probably without the microscopic coexistence of magnetism and superconductivity[32-34]. Our Ca(Fe$_{1-x}$Co$_x$)$_2$As$_2$ samples are cleaved in cryogenic ultrahigh vacuum and then inserted into the STM head; all data reported here were acquired at 4.2 K. The surfaces are atomically flat and exhibit a 1×2 surface reconstruction at ~45° to both the a and b axes, which we have previously demonstrated to have no impact on accurate visualization of FeAs plane electronic structure[26]. We image the differential tunnelling conductance $dI/dV(\mathbf{r}, E = eV) \equiv g(\mathbf{r}, E)$ with atomic resolution and register, as a function of both location $\mathbf{r}$ and electron energy E. The Fourier transform of
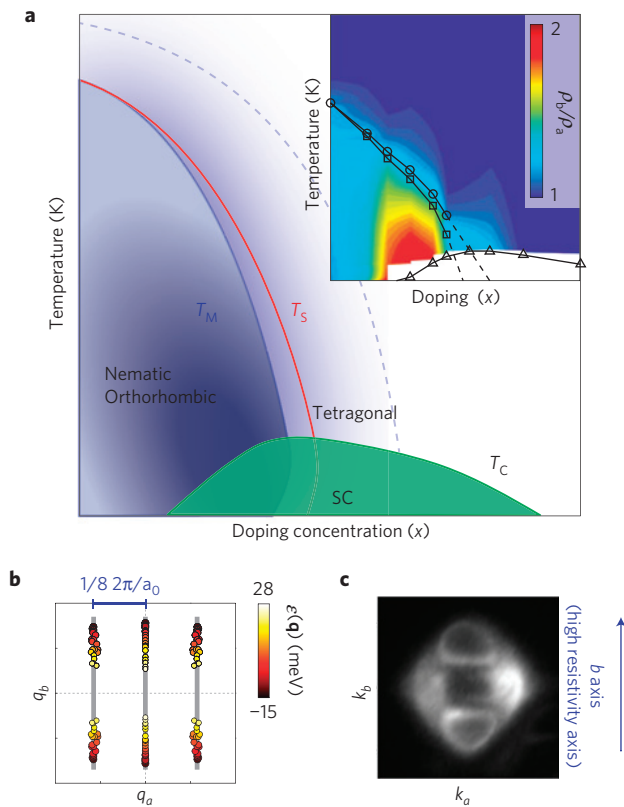
Figure 1 | Anisotropic transport and QPI in underdoped iron-based superconductors. a, Schematic phase diagram of $A(Fe_{1-x}Co_x)_2As_2$ (A = Ca, Sr and Ba) as a function of doping concentration x including the structural T_S, magnetic T_M and superconducting T_C transition temperatures. Note that the phase diagrams are slightly different, depending on the transition metal A; for example the coexistence between superconductivity and magnetism seen in Ba-122 is probably absent in Ca-122 (see text)[32–34]. The dashed line indicates nematic putative fluctuations. Inset: the evolution of the in-plane resistivity anisotropy as a function of temperature and doping, expressed in terms of the resistivity ratio ρ_b/ρ_a (reproduced with permission from ref. 14). **b**, The unidirectional dispersion of the six QPI peaks occurs along the b axis only[26] with two 'satellites' of the central unidirectional dispersion shifted by $\Delta q \approx 1/8a_0$. **c**, Photocurrent intensity at the Fermi level ($E = 0$) of Ca-122 measured by ARPES (from ref. 30). **b,c** are oriented so that the crystal b axis points vertically.

$g(\mathbf{r}, E), g(\mathbf{q}, E)$, is then used to determine the characteristic wave vectors of dispersive modulations due to quasiparticle scattering interference (QPI). As shown in Fig. 1b, these patterns exhibit[26] a strongly unidirectional hole-like dispersion along the b axis only, with two apparent 'satellites' of the basic unidirectional dispersion characteristics shifted by $\delta q \cong \pm 2\pi/8a_0$ along the a axis. Importantly, without the Co-dopant atoms at $x = 0$, these QPI effects are absent[26] (Supplementary Section SI). At finite doping, the observed quasiparticle interference pattern (Fig. 1b) is highly inconsistent with predictions using the relevant Fermi surface of the same material shown in Fig. 1c (Fig. 3a,b and Supplementary Section SII). Finally, if one interpreted these observations as the preferential propagation of delocalized electrons along the b axis, this would be highly inconsistent with the d.c. electrical transport and ACT studies[14–25] reporting that the low-resistance transport always occurs along the a axis. An explanation for all these apparently contradictory phenomena is required.

These QPI effects coexist with intense but poorly understood static electronic disorder at the nanoscale[26]. Figure 2a shows a

typical topographic image of the cleaved surface of underdoped Ca-122 whereas Fig. 2b is the simultaneously acquired current image of non-dispersive states achieved by integrating the electronic structure images over energy $I(\mathbf{r}, -37\,\text{meV}) = \int_0^{E \approx -37\,\text{meV}} g(\mathbf{r}, \omega)\,\text{d}\omega$ to remove dispersive effects. This shows vividly the energetically quasi-static electronic disorder strongly oriented along the a axis. To explore the nanoscale constituents of this disorder, we carry out an autocorrelation analysis of $I(\mathbf{r}, E)$, as shown in Fig. 2c. Although this reveals no periodic modulations in the static electronic disorder, there is a sharply defined structure surrounding the centre of the autocorrelation. The inset to Fig. 2c, showing its full details, reveals that, beyond the required central peak, there are two peaks along the a axis, which are separated from the central point by a distance of $|\mathbf{d}| = 22\,\text{Å} \approx 8a_0$ (Supplementary Section SII). The absence of other features in the autocorrelation demonstrates that $|\mathbf{d}|$ is the only persistence length. Figure 2d shows the Fourier transform of Fig. 2b, from which we conclude that there is no periodicity whatsoever (thus excluding periodic 'stripes' as the explanation).

We next consider what type of nanoscale phenomenon could generate all the effects in Fig. 2b–d. We analyse a model hypothesizing identical, co-oriented but otherwise randomly located, anisotropic impurity states. The inset to Fig. 2e shows a model impurity state in real space in the shape of a 'dimer'. This can be parameterized using two Gaussians $C_\sigma(\mathbf{r}) = c_0(e^{-|\mathbf{r}|^2/\sigma^2})$ separated from each other by a distance $|\mathbf{d}| = 22\,\text{Å} \approx 8a_0$ where $\mathbf{d}$ is always parallel to the a axis, so that the complete impurity state is modelled by $D(\mathbf{r}) = C_\sigma(\mathbf{r}+\mathbf{d}/2) + C_\sigma(\mathbf{r}-\mathbf{d}/2)$. We then consider a randomly distributed ensemble of such co-oriented anisotropic impurity states, as would be observable in the energy-integrated tunnel-current map $I(\mathbf{r})$. The left-hand panel of Fig. 2e shows four such impurity states at random locations exemplifying the basic structure of our model. The right-hand panel shows the effect of ~47 such states distributed at random. Figure 2f shows results from precisely the same model, but now with 1,000 a axis oriented anisotropic impurity states—the approximate number of Co-dopant atoms within this field of view (FOV) at $x \sim 3.0\%$ (Supplementary Section SIV). A comparison with Fig. 2b reveals the strong consistency between the predictions from this model and our experimental observations. Figure 2g is the autocorrelation of Fig. 2e and exhibits the identical central feature. The comparison between the central features in inset Fig. 2c (experiment) and inset Fig. 2g (model) is very good. Finally Fig. 2h shows the Fourier transform of the simulation in Fig. 2f; it lacks any peaks that would indicate a periodic structure. Once again, the correspondence between the experimental result in Fig. 2d and the model simulation in Fig. 2h is excellent. In summary: the correspondences between Fig. 2b and f, c and g, and d and h respectively, provide compelling evidence that the static electronic disorder in underdoped Ca-122 indeed consists of a randomly distributed ensemble of a axis oriented electronic anisotropic impurity states, all of size $|\mathbf{d}| = 22\,\text{Å} \approx 8a_0$.

Another key observation is shown in the inset to Fig. 2b (Supplementary Sections SV and SVI). Here the electronic structure surrounding every observed Co-dopant atom location[2,26] is demonstrated. This is identified by averaging the measured $I(\mathbf{r}, E)$ over many small fields of view, with each being centred on a Co substitution site, to yield $\langle I(\mathbf{r}, E) \rangle_{Co}$. We see directly that two peaks exist in $\langle I(\mathbf{r}, E) \rangle_{Co}$, each separated from the dopant-atom site (red+) by $\pm \mathbf{d}/2$. These data provide direct atomic-scale evidence that Co-dopant atoms play a central role in either the establishment or pinning of the observed anisotropic impurity states.

The existence of such highly anisotropic impurity states can be expected to influence various aspects of the physics of underdoped FeAs materials. Perhaps most importantly, it has been proposed that such impurity states scatter quasiparticles anisotropically and thus contribute significantly to the nematic transport[7,8,12,22,23]. Generally, electronic transport can be described by the Boltzmann
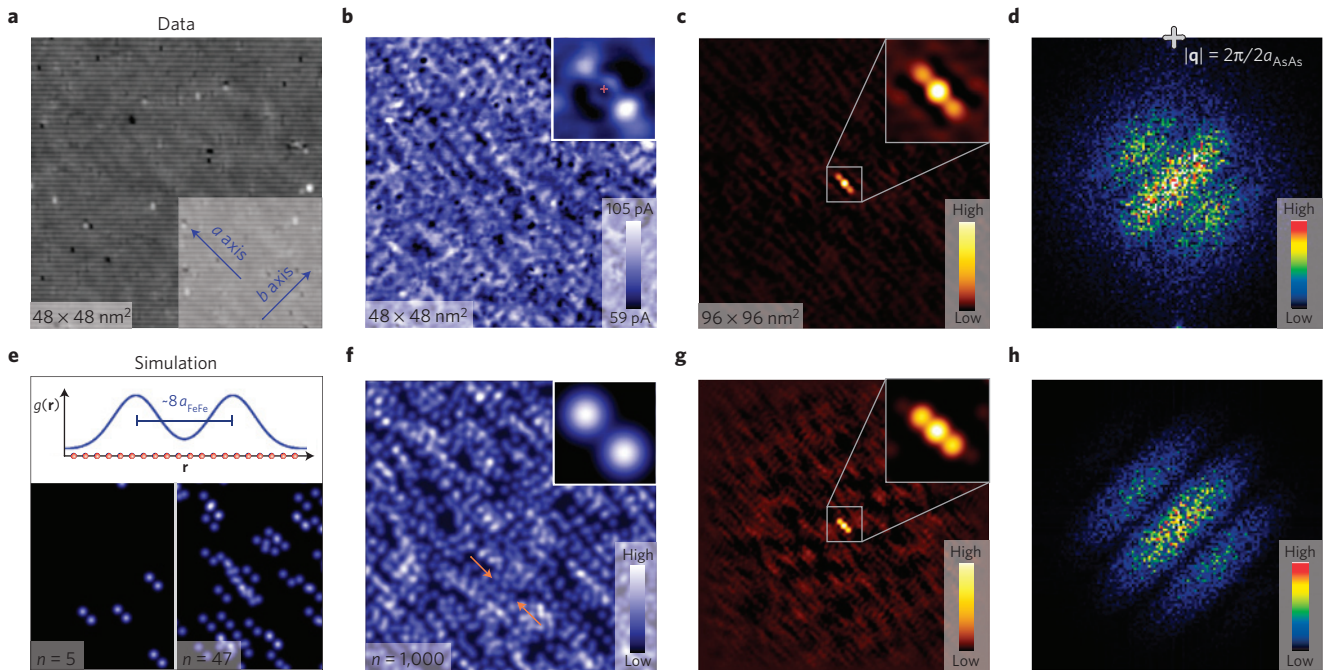
Figure 2 | Visualizing the anisotropic impurity state structure in Ca-122. a, A 48 nm × 48 nm topographic image of the Ca-122 surface, taken simultaneously with the measurements depicted in **b–d**. The horizontal lines stem from a surface reconstruction and do not influence our ability to visualize the correct FeAs electronic structure; the orientations of crystal axes are identified. **b**, The simultaneously recorded non-dispersive component in the electronic structure as determined the current map $I(\mathbf{r}, E)$ at $E = -37$ meV. The inset shows the characteristic non-dispersive electronic structure environment of a typical Co-dopant atom (see Supplementary Sections SV and SVI): it is observed directly to be a 'dimer'-shaped electronic impurity state. **c**, The autocorrelation of $I(\mathbf{r}, -37$ meV) shows three peaks separated by the characteristic length scale of 22 Å. Note that, apart from the triple-peak, the $AC\{I(\mathbf{r}, -37$ meV)$\}$ signal is low, proving that 22 Å is the only persistent length scale in the image. **d**, Fourier transform $I(\mathbf{q}, -37$ meV) of the image shown in **b**. No sharp peaks indicating a periodic structure are seen anywhere in reciprocal space. **e**, Inset, the proposed impurity state with the Fe-lattice for comparison. The lower half show simulations with $n = 5$ and $n = 47$. **f**, A simulation with $n = 1,000$ anisotropic impurity states in the same 48 nm × 48 nm FOV (Supplementary Section SIV); their centres are randomly distributed but they are all aligned with the a axis. This 'glassy' pattern of overlapping anisotropic impurity states looks similar to the data shown in **b–d**. The autocorrelation and Fourier transform (**g,h**) of the image in **f** support the validity of our deduction that the static electronic disorder consists of a axis oriented electronic anisotropic impurity states only.

transport equation, which allows for two rotational symmetry breaking terms: the Fermi velocities, $v_F(\mathbf{k})$, and the scattering probabilities, $W(\mathbf{k}, \mathbf{k}')$. Some proposals have concentrated on the Fermi velocity anisotropy, and assumed that a rigid band shift leads to a change thereof on doping[20]. Here, however, we explore the complementary proposals that it is anisotropic scattering that contributes significantly to the nematic transport. Quasiparticle interference imaging can investigate such proposals because it directly measures the scattering of quasiparticles. For a point scatterer in the Born approximation, the power-spectral-density in differential conductance shows modulations due to QPI, $P(\mathbf{q}, E) \propto g(\mathbf{q}, E)$ can be determined from[35]

$$P(\mathbf{q}, E) = \frac{1}{N} \left| \frac{1}{\pi} \mathrm{Im}\Lambda(\mathbf{q}, E) \right|^2 |\delta\varepsilon(\mathbf{q})|^2 \qquad (1)$$

Here the term $|(1/\pi)\mathrm{Im}\Lambda(\mathbf{q}, E)|^2$, with Λ being a specific convolution of Green's functions $\Lambda(\mathbf{q}, E) \equiv \int d^2 r e^{i\mathbf{q}\cdot\mathbf{r}} G(\mathbf{r}, E) G(-\mathbf{r}, E)$, represents the 'bare' QPI signature expected from a point scatterer within the native band structure. The $|\delta\varepsilon(\mathbf{q})|^2$ term is the square of the structure factor (Fourier transform of the $\mathbf{r}$-space scattering potential) of any non-point-like scattering centre. Of most significance here, equation (1) describes the simplest way that an anisotropic scatterer should influence the QPI data, being the product of the 'bare' QPI signal and the square of the structure factor of the anisotropic scatterer.

If the spatial extent of each scatterer in $Ca(Fe_{1-x}Co_x)_2As_2$ is modelled by a delta function in $\mathbf{r}$-space and the measured $A(\mathbf{k}, E)$ of

that material is used to model Fermi surface and band dispersions (Supplementary Section SII), this predicts the $P(\mathbf{q}, E = 0)$ as shown in Fig. 3a. In Fig. 3b, we show the measured $g(\mathbf{q}, E = 0)$, which are obviously strongly inconsistent with Fig. 3a. One might therefore be tempted to deduce that the reported QPI data are artefacts unrelated to the fundamental FeAs band structure. However, if the scattering centres exhibit the structure factor of the model anisotropic impurity state (Fig. 2e):

$$|\delta\varepsilon(\mathbf{q})| = |FT\{C_\sigma(\mathbf{r} - \mathbf{d}/2) + C_\sigma(\mathbf{r} + \mathbf{d}/2)\}|$$
$$\propto 2|\cos(\mathbf{d}\cdot\mathbf{q}/2)|C_{1/\sigma}(\mathbf{q}) \qquad (2)$$

we find a very different conclusion. Figure 3c shows the predicted QPI patterns for underdoped Ca-122, again using the native $A(\mathbf{k}, E)$ as measured by ARPES, but now in combination with the structure factor from equation (2), to predict $\Lambda(\mathbf{q}, E)$. Here we find three parallel lines separated from each other by $\delta\mathbf{q} \cong \pm 2\pi/8a_0$ and all dispersing identically on the same trajectory of Fig. 1b (or red line in Fig. 3d), so that the equivalent agreement between Fig. 3b,c holds for all energies. Thus we show that, for Ca-122, the $A(\mathbf{k}, E)$ from ARPES and the observed QPI are actually rather consistent with each other if dopant-induced $\sim 8a_0$ anisotropic impurity states act as the predominant scatterers.

Conversely, QPI measurements can be used to measure directly the actual scattering characteristics of impurity states in Ca-122. Figure 4b shows the angular dependence of the quasiparticle scattering rate determined using the square of the structure factor of
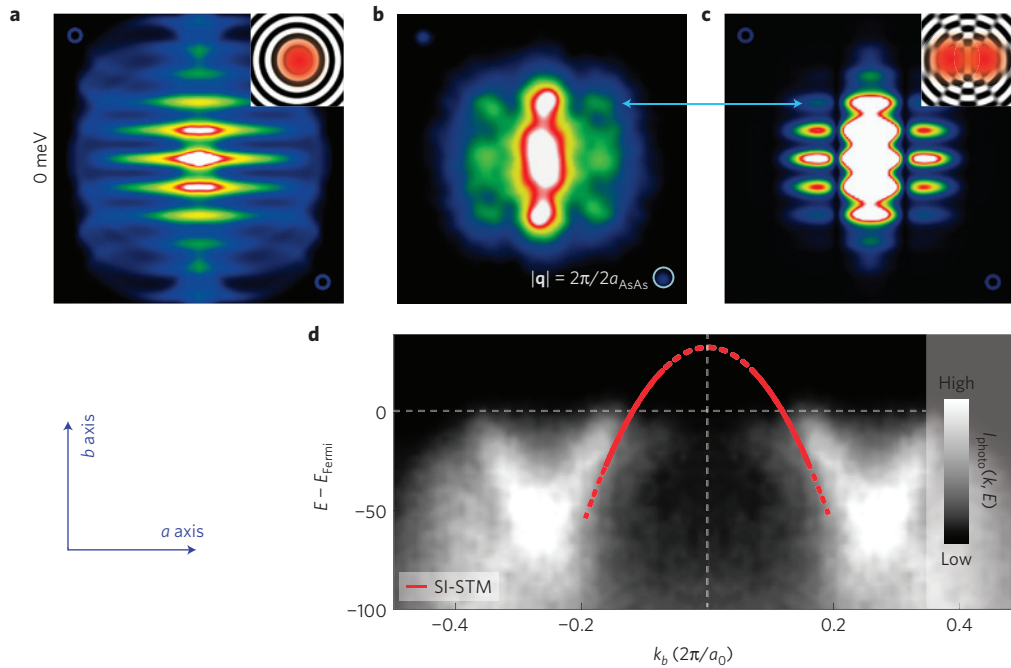
Figure 3 | Anisotropic QPI from anisotropic impurity states. (See Supplementary Section SVII for a comparison of **q**- and **k**-space.) **a**, The QPI pattern one would expect from the ARPES band structure (Fig. 1e and Supplementary Section SII) with the quasiparticles scattering from point-like scatterers. **b**, The QPI pattern as measured in Ca-122 in the same energy range. Although the dispersion is correct, there are clear vertical lines of suppressed intensity in the data, which are not visible in the simulations. **c**, Using the structure factor of a 'dimer' (Fig. 2) impurity state, the calculations yield QPI predictions consistent with the data in **b** (see for example blue line). **d**, The dispersion of the measured QPI (red line) is in agreement with the dispersion determined by ARPES (photocurrent intensity in grey scale).
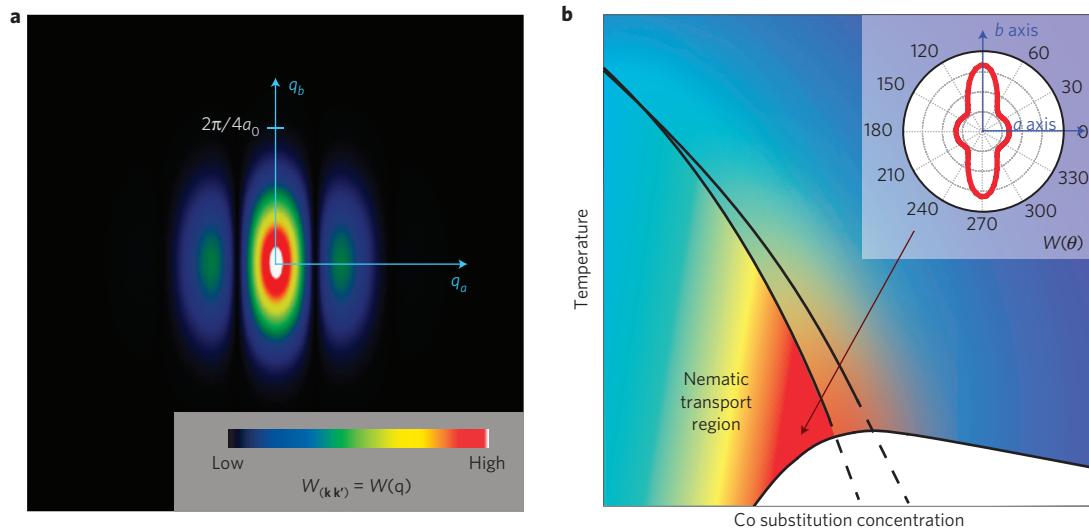

Figure 4 | Anisotropic transport due to scattering from anisotropic impurity states. a, False colour plot of the probability for a state **k** to scatter into a state **k**′, which in the Born approximation using plane waves is proportional to the Fourier transform of the scattering potential $W(\mathbf{k},\mathbf{k}') = W(\mathbf{q}) \sim |FT\{V(\mathbf{r})\}|^2$. We take the scattering potential to have the same spatial form as the observed anisotropic impurity states (Fig. 2), with parameters for our model obtained from the experimental data. This then leads to the depicted C_2-symmetric scattering probability $W(\mathbf{q} = \mathbf{k} - \mathbf{k}')$. **b**, A schematic phase diagram of 122 FeAs superconductors with increasingly nematic transport is indicated by blue, yellow and red colours, where the latter marks strongest transport anisotropy. To emphasize the directional dependence of the scattering probability from our QPI data, we plot in the inset the cumulative scattering probability in a given direction $\theta = \angle(\mathbf{k},\mathbf{k}')$. This is obtained by integrating over the radial coordinate: $W(\theta) = \int d|\mathbf{q}|W(\theta,|\mathbf{q}|)$ in **a**. Note the strong scattering maxima along the b axis.

the observed anisotropic impurity states (Fig. 4a). It is clearly highly anisotropic and its maximum |**q**|-integrated intensity is found to occur along the b axis. Although applications of the Boltzmann transport equation can be complex and do depend on the Fermi surface, our analysis nevertheless provides a plausible explanation

for how the scattering rates of the anisotropic impurity states (Figs 2 and 3) should affect the transport nematicity.

Overall, our data demonstrate that insertion of Co-dopant atoms on the Fe sites in Ca-122 generates a dense ensemble of $\sim 8a_0$ long highly anisotropic impurity states (Fig. 2). Because their a

axis oriented extended structure (Fig. 2) is observed within the strongly anisotropic magnetic environment, it seems plausible that these anisotropic impurity states are locally magnetic in origin[5,6]. Notwithstanding their microscopic mechanism, the measured characteristics of these dopant-induced impurity states can provide a simple yet comprehensive explanation for both the complex QPI phenomenology[26] and the transport anisotropy[14–25] of underdoped iron-superconductors. This is because scattering of quasiparticles from such impurity states is demonstrably highly anisotropic, with its maximum rate along the b axis (Figs 3 and 4). Finally, on the basis of this example, it seems plausible that equivalent atomic-scale electronic phenomena can play an important role in the phase diagrams of other correlated-electron materials when dopant atoms are introduced.

References

1. Paglione, J. & Greene, R. L. High-temperature superconductivity in iron-based materials. *Nature Phys.* **6,** 645–658 (2010).
2. Kemper, A. F., Cao, C., Hirschfeld, P. J. & Cheng, H-P. Effects of cobalt doping and three-dimensionality in BaFe$_2$As$_2$. *Phys. Rev. B* **80,** 104511 (2009).
3. Wadati, H., Elfimov, I. & Sawatzky, G. A. Where are the extra d electrons in transition-metal-substituted iron pnictides? *Phys. Rev. Lett.* **105,** 157004 (2010).
4. Nakamura, K., Arita, R. & Ikeda, H. First-principles calculation of transition-metal impurities in LaFeAsO. *Phys. Rev. B* **83,** 144512 (2011).
5. Zhou, T. *et al.* Quasiparticle states around a nonmagnetic impurity in electron-doped iron-based superconductors with spin-density-wave order. *Phys. Rev. B* **83,** 214502 (2011).
6. Chen, C-C. *et al.* Revealing the degree of magnetic frustration by non-magnetic impurities. *New J. Phys.* **13,** 043025 (2011).
7. Fernandes, R. M., Abrahams, E. & Schmalian, J. Anisotropic in-plane resistivity in the nematic phase of the iron pnictides. *Phys. Rev. Lett.* **107,** 217002 (2011).
8. Inoue, Y., Yamakawa, Y. & Kontani, H. Impurity-induced electronic nematic state in iron-pnictide superconductors. *Phys. Rev. B* **85,** 224506 (2012).
9. Konbu, S., Nakamura, K., Ikeda, H. & Arita, R. Fermi-surface evolution by transition-metal substitution in the iron-based superconductor LaFeAsO. *J. Phys. Soc. Jpn* **80,** 123701 (2011).
10. Huang, H., Gao, Y., Zhang, D. & Ting, C. S. Impurity-induced quasiparticle interference in the parent compounds of iron-pnictide superconductors. *Phys. Rev. B* **84,** 134507 (2011).
11. Levy, G. *et al.* Probing the role of Co substitution in the electronic structure of iron pnictides. *Phys. Rev. Lett.* **109,** 077001 (2012).
12. Kang, J. & Tešanović, Z. Anisotropic impurity scattering, reconstructed Fermi-surface nesting, and density-wave diagnostics in iron pnictides. *Phys. Rev. B* **85,** 220507(R) (2012).
13. Vavilov, M. G. & Chubukov, A. V. Phase diagram of iron pnictides if doping acts as a source of disorder. *Phys. Rev. B* **84,** 214521 (2011).
14. Chu, J-H. *et al.* In-plane resistivity anisotropy in an underdoped iron arsenide superconductor. *Science* **329,** 824–826 (2010).
15. Tanatar, M. A. *et al.* Uniaxial-strain mechanical detwinning of CaFe$_2$As$_2$ and BaFe$_2$As$_2$ crystals: Optical and transport study. *Phys. Rev. B* **81,** 184508 (2010).
16. Ishida, S. *et al.* Manifestations of multiple-carrier charge transport in the magnetostructurally ordered phase of BaFe$_2$As$_2$. *Phys. Rev. B* **84,** 184514 (2010).
17. Dusza, A. *et al.* Anisotropic charge dynamics in detwinned Ba(Fe$_{1-x}$Co$_x$)$_2$As$_2$. *Euro. Phys. Lett.* **93,** 37002 (2011).
18. Nakajima, M. *et al.* Unprecedented anisotropic metallic state in undoped iron arsenide BaFe$_2$As$_2$ revealed by optical spectroscopy. *Proc. Natl Acad. Sci. USA* **108,** 12238–12242 (2011).
19. Blomberg, E. C. *et al.* In-plane anisotropy of electrical resistivity in strain-detwinned SrFe$_2$As$_2$. *Phys. Rev. B* **83,** 134505 (2011).
20. Kuo, H-H. *et al.* Possible origin of the nonmonotonic doping dependence of the in-plane resistivity anisotropy of Ba(Fe$_{1-x}$T$_x$)$_2$As$_2$ (T = Co, Ni and Cu). *Phys. Rev. B* **84,** 054540 (2011).
21. Ying, J. J. *et al.* Measurements of the anisotropic in-plane resistivity of underdoped FeAs-based pnictide superconductors. *Phys. Rev. Lett.* **107,** 067001 (2011).
22. Ishida, S. *et al.* In-plane resistivity anisotropy induced by impurity scattering in the magnetostructural ordered phase of underdoped Ba(Fe$_{1-x}$Co$_x$)$_2$As$_2$. Preprint at http://arXiv.org/abs/1208.1575 (2012).
23. Nakajima, M. *et al.* Effect of Co doping on the in-plane anisotropy in the optical spectrum of underdoped Ba(Fe$_{1-x}$Co$_x$)$_2$As$_2$. *Phys. Rev. Lett.* **109,** 217003 (2012).
24. Chu, J-H. *et al.* Divergent nematic susceptibility in an iron arsenide superconductor. *Science* **337,** 710–712 (2012).
25. Wang, A. F. *et al.* Electronic nematicity in pseudogap-like phase diagram of NaFe$_{1-x}$Co$_x$As. Preprint at http://arXiv.org/abs/1207.3852v1 (2012).
26. Chuang, T-M. *et al.* Nematic electronic structure in the parent state of the iron-based superconductor Ca(Fe$_{1-x}$Co$_x$)$_2$As$_2$. *Science* **327,** 181–184 (2010).
27. Song, C. L. *et al.* Direct observation of nodes and twofold symmetry in FeSe superconductor. *Science* **332,** 1410–1413 (2011).
28. Zhou, X. *et al.* Quasiparticle interference of C_2-symmetric surface states in a LaOFeAs parent compound. *Phys. Rev. Lett.* **106,** 087001 (2011).
29. Kasahara, S. *et al.* Electronic nematicity above the structural and superconducting transition in BaFe$_2$(As$_{1-x}$P$_x$)$_2$. *Nature* **486,** 382–385 (2012).
30. Wang, Q. *et al.* Uniaxial 'nematic-like' electronic structure and Fermi surface of untwinned CaFe$_2$As$_2$. Preprint at http://arxiv.org/abs/1009.0271 (2010).
31. Yi, M. *et al.* Symmetry breaking orbital anisotropy on detwinned Ba(Fe$_{1-x}$Co$_x$)$_2$As$_2$ above the spin density wave transition. *Proc. Natl Acad. Sci. USA* **108,** 6878–6883 (2011).
32. Ni, N. *et al.* First-order structural phase transition in CaFe$_2$As$_2$. *Phys. Rev. B* **78,** 014523 (2008).
33. Harnagel, L. *et al.* Phase diagram of the iron arsenide superconductors Ca(Fe$_{1-x}$Co$_x$)$_2$As$_2$ ($0 = x = 0.2$). *Phys. Rev. B* **83,** 094523 (2008).
34. Ran, S. *et al.* Control of magnetic, nonmagnetic, and superconducting states in annealed Ca(Fe$_{1-x}$Co$_x$)$_2$As$_2$. *Phys. Rev. B* **85,** 224528 (2012).
35. Capriotti, L., Scalapino, D. J. & Sedgewick, R. D. Wave-vector power spectrum of the local tunneling density of states: Ripples in a d-wave sea. *Phys. Rev. B* **68,** 014508 (2003).

Author contributions

M.P.A. and T-M.C. carried out the SI-STM experiments with contributions from F.M.; N.N., S.L.B. and P.C.C. synthesized and characterized the sequence of samples; Q.W. and D.S.D. were responsible for the ARPES work and analysis; M.P.A. proposed the anisotropic impurity states and performed the subsequent SI-STM data analysis and figure development; J.C.D. and M.P.A. wrote the paper with contributions from F.M., T-M.C., M.S.G., G.S.B., D.S.D. and Y.X.; J.C.D. supervised the project. The manuscript reflects the contributions and ideas of all authors.

Additional information

Supplementary information is available in the online version of the paper. Reprints and permissions information is available online at www.nature.com/reprints. Correspondence and requests for materials should be addressed to J.C.D.

Competing financial interests

The authors declare no competing financial interests.